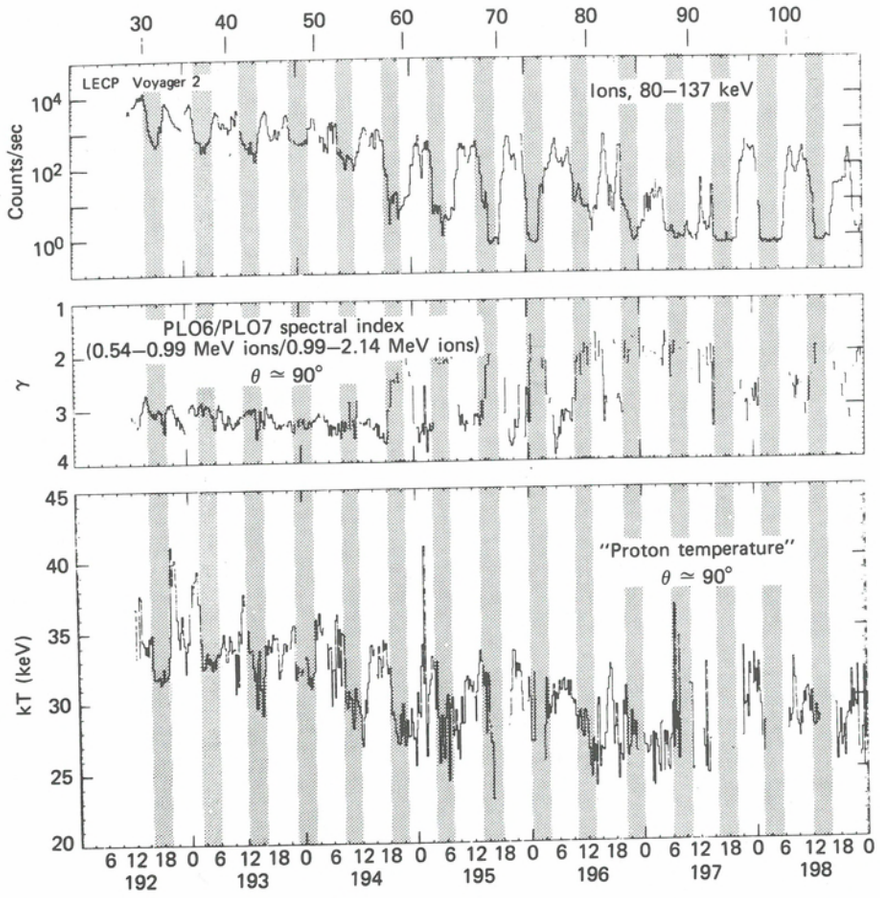

Fig. 4.18. Similar to Figure 4.17 but for Voyager 2 outbound [Krimigis et al., 1981].

Figure 4.18 shows the variation of spectral parameters for Voyager 2 for the outbound trajectory to $\sim 105\ R_J$. The γ parameter displays little variation with distance from the magnetodisc through late on day 194, at which time the spectrum becomes much harder outside the magnetodisc, due to the presence of solar energetic protons on nightside field lines [Hamilton et al., 1981]. The temperature profile shown in the lower panel, however, closely follows the intensity profiles on the top panel; that is, temperature peaks occur at density maxima and temperature valleys occur at density minima. Although spectral data are not shown for the magnetospheric wind region (i.e, after day 203), the values for γ and kT are in the same range as those determined for the magnetodisc.

The presentation of the spectra would be incomplete without some indication of the behavior of energetic electrons. Figure 4.19 shows representative differential spectra (upper panel) at low energies for selected time intervals (lower panels) during the inbound pass of Voyager 1. The data points are plotted at the geometric mean for each of the five differential channels of the low-energy electron detector. The spectra can be described by $dj/dE = KE \exp(-E/E_0)$ with values of E_0 ranging from 25 to 35 keV. Note that if E_0 is interpreted as kT, the temperatures are quite similar to those obtained

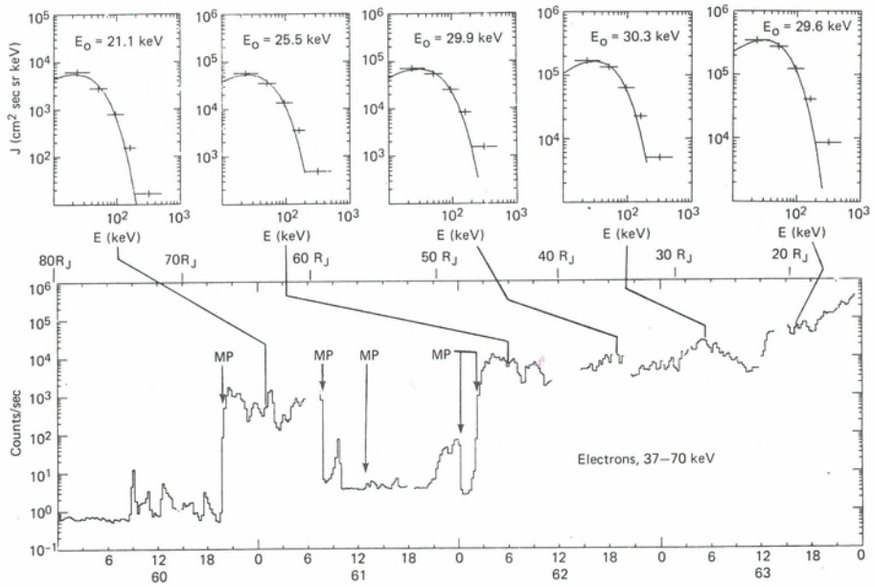

Fig. 4.19. Characteristic spectra of low energy electrons in outer magnetosphere. Lower panel shows detailed intensity profile. Upper panels show spectral plots at the indicated times. "Goodness of fit" to a γ-thermal spectrum is typically ~ 0.08 in fitting the thermal part to the lowest three points.

for the ions. Further, there is a tendency for E_0 to increase as the distance to the planet decreases. A more detailed investigation [Carbary and Krimigis, 1980] has shown that a pure exponential is an equally good fit and is characteristic of both the dayside and nightside magnetosphere.

Number-density and pressure profiles. A lower bound on the number density of energetic ions can be obtained from the measured differential intensities using relation (4.23) of Appendix C:

$$\mathbf{N} > \sum_{\mathbf{n}} \sum_{k} \frac{2\pi \Delta\mu_n}{G v_k} R_k(\mathbf{n}) \tag{4.13}$$

$R_k(\mathbf{n})$ is the rate measured by the k^{th} energy channel (geometric factor G) in the solid angle $2\pi\ \Delta\mu_n$ about the unit vector $(-\mathbf{n})$; see the definition of R_k in (4.17) of Appendix A. The lower bound is valid if the "scaling velocity" v_k for the k^{th} channel satisfies the condition (4.22) of Appendix C. The density lower bound calculated in this manner is independent of any model, makes use of the observed differential intensity and angular distribution, and only depends on the selection of v_k, which represents the velocity of a specific ion in a particular energy channel. To obtain a lower limit on the number density, we assume that the detector response in all directions is entirely due to protons; in this case the velocity we use in Equation (4.13) is that appropriate for the proton energy passband of each particular channel. The likely upper bound on the densities is obtained by assuming that the detector responds entirely to oxygen in every direction; that is, the velocity used in the denominator of Equation (4.13) is that appropriate for oxygen ions in each channel. See Krimigis et al. [1981] and the derivation of Equation (4.23) in Appendix C for further discussion.

The computation of a lower bound on the average energetic (i.e., $\gtrsim 30$ keV) particle pressure $\overline{P}$ can be done in a similar manner to that employed in the computation of particle density, that is, by simple integration of the observed spectra, and is given by expression (4.29) of Appendix C:

$$\overline{P} > \sum_k \frac{4\pi p_k}{3G} R_k(\mathbf{n}_\perp) \tag{4.14}$$

where p_k is a scaling momentum, not necessarily related to the quantity v_k in (4.13), and the rate of the k^{th} channel is now taken only in the direction ($\mathbf{n}_\perp$) perpendicular to the convection velocity. The quantities in the summation are known or observable, and we proceed to obtain a lower and upper limit on the pressure in a manner similar to that of the density by using the appropriate p_k for a particular channel. This approximation is closely related to the stricter lower bound on pressure given by Equation (4.23) in Appendix C, which is valid if condition (4.28) is satisfied. The number density and pressure profiles for the encounter of Voyager 2 are presented in the next three figures.

Figure 4.20 shows density and pressure data for the inbound portion of the Voyager 2 trajectory through $\sim 30\ R_J$. Estimated electron densities from the plasma wave (PWS) instrument [Gurnett et al., 1981b], and ion densities from the plasma (PLS) instrument are shown for comparison. It is evident that there appear to be significant differences between the LECP densities and the PWS electron densities at the magnetopause encounters at ~ 72 and $\sim 62\ R_J$. However, from the second magnetopause crossing and to distances as close as 45 R_J, there is reasonable agreement between the energetic particle ion concentrations and the PWS electron concentrations, given the limitations of this comparison [for a full discussion see Krimigis et al., 1981].

Inside $\sim 45\ R_J$ there are significant increases in the electron concentrations that are not reflected in the energetic ion concentrations, especially at 43 and 39 R_J and most importantly $\sim 33\ R_J$. We note that during this last electron concentration enhancement, the low-energy plasma densities from Belcher, Goertz, and Bridge [1980] appear to agree well with the PWS data, suggesting that at these times copious fluxes of ions were present with energies below the LECP energy threshold. The bottom panel of Figure 4.20 shows the particle pressure profile, including the comparison with magnetic field energy density. It is observed that energetic particle pressure can easily balance the magnetic field pressure and that the field energy density is generally depressed during energetic particle pressure peaks. This appears to be the case even during electron concentration peaks at ~ 43, ~ 38, and $\sim 33\ R_J$, suggesting that even at those times when the cold plasma appears to dominate, the pressure is carried entirely by the energetic particles.

The presentation of the number-density and pressure profile is continued in Figure 4.21 although the LECP instrument was in its stow mode [for assumptions regarding the derivation of these densities see Krimigis et al., 1981]. It is evident that electron densities reported by the PWS near closest approach are generally higher than the ion densities derived from the LECP measurements. Gurnett et al. [1981b] find that there is good agreement between the energetic particle densities and those obtained by the plasma wave instrument, if the assumption is made that the LECP detector response is primarily due to doubly ionized oxygen.

The lower panel shows energetic particle pressure compared to the observed and expected magnetic field signatures, from the work of Ness et al. [1979c]. It is evident from the data that the large diamagnetic depressions observed at ~ 1100 and ~ 2200 UT on day 190 and ~ 1000 UT on day 191, are coincident with large peaks in the ener-

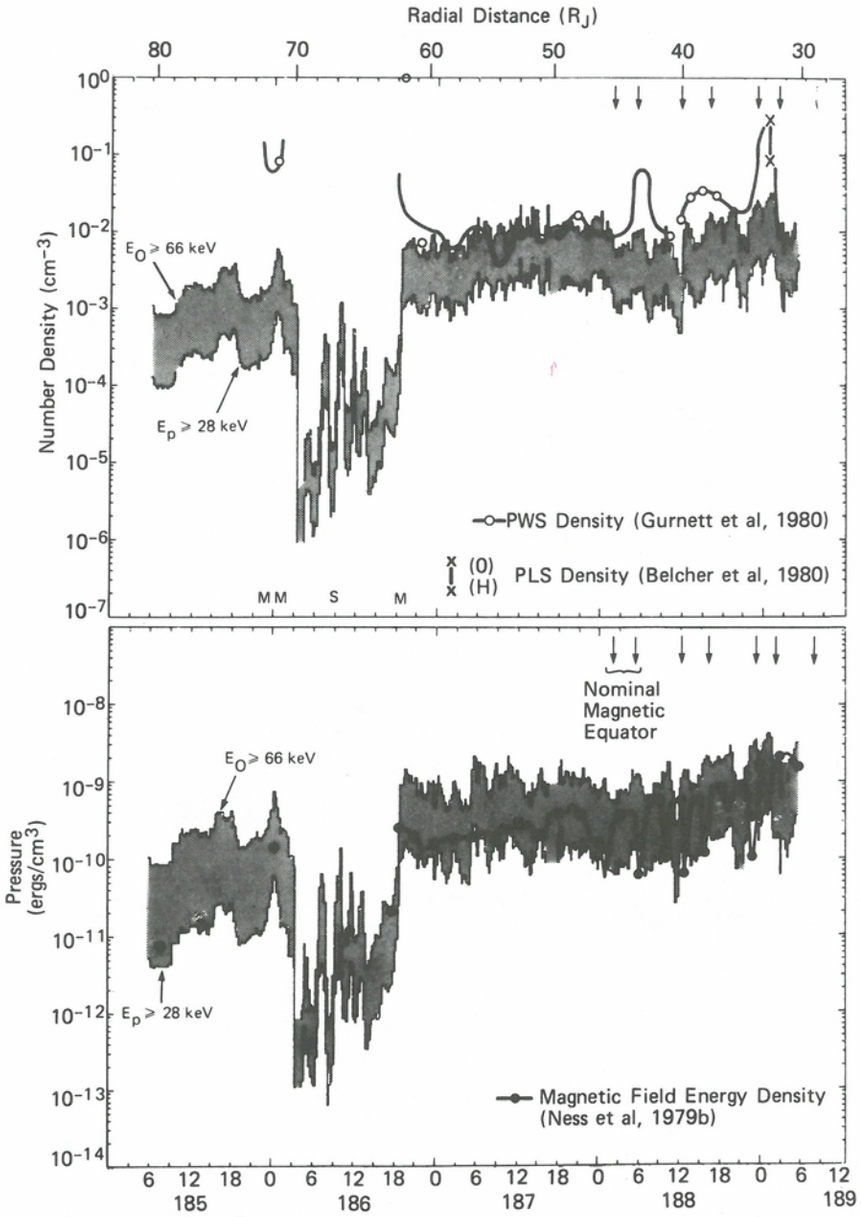

Fig. 4.20. Voyager 2 inbound ion density and pressure [Krimigis et al., 1981]. Shown are the computed density (top panel) and pressure (bottom panel) derived from an integration of the observed spectra. The upper curve corresponds to the assumption that all particles are singly charged oxygen and the lower curve to the assumption that all particles are protons. In the top panel, the bow shock (*S*) and the magnetopause (*M*) are indicated; crossings of the nominal magnetic equator are indicated by the short arrows. The solid line indicates the electron density derived from the plasma wave experiment with the open points representing exact density determinations. The crosses are plasma densities from the plasma experiment. The solid line in the lower panel indicates the magnetic field energy density ($B^2/8\pi$) obtained from the magnetic field experiment [Ness et al., 1979c].

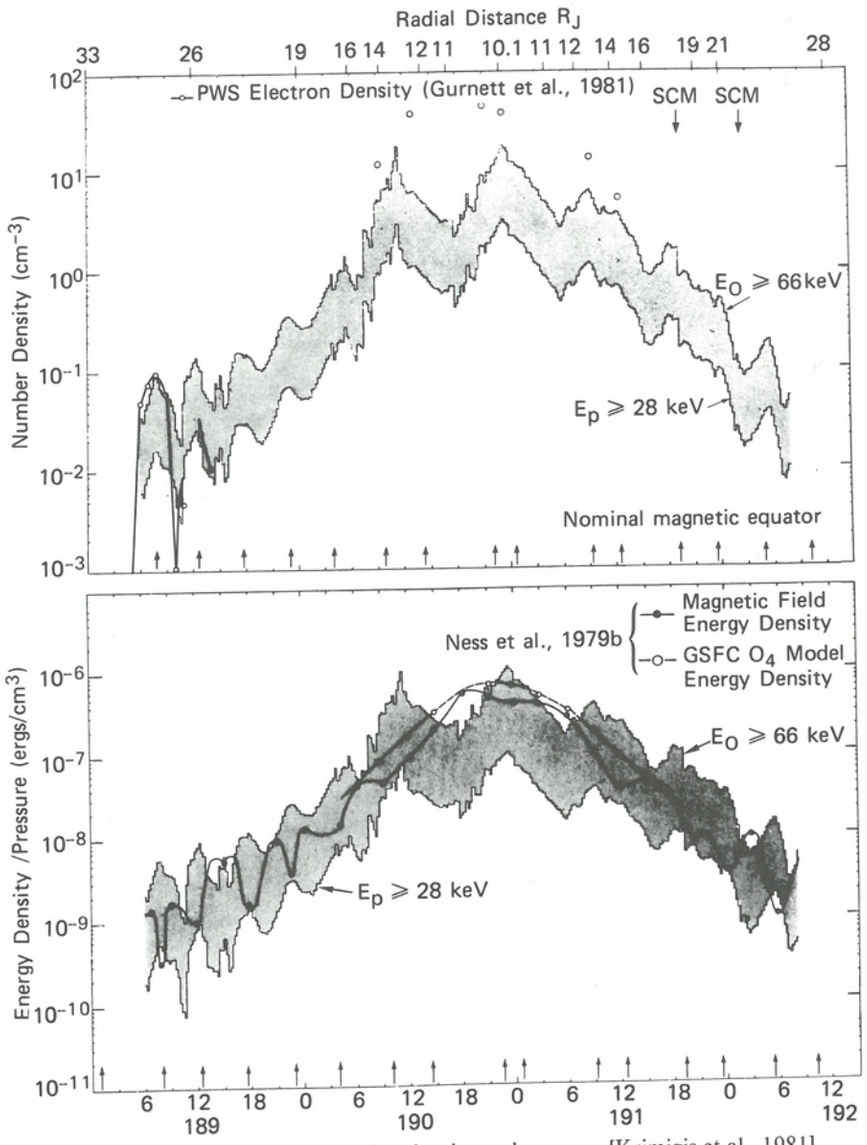

Fig. 4.21. Voyager 2 near encounter ion density and pressure [Krimigis et al., 1981]. SCM denotes a spacecraft maneuver.

getic particle pressure. In addition to the main peaks, good correlation between energetic-particle-pressure maxima and magnetic-field depressions are found both prior to and well after closest approach.

To summarize, it appears that for the duration of the entire Voyager 2 inbound pass the plasma pressure can be accounted for with ions of energies $\gtrsim 30$ keV, that is, a situation that also obtains in the Earth's ring current [Williams, 1979]. With regard to particle number density, it is evident that a large fraction of the density in the outer magnetosphere ($\gtrsim 40\ R_J$) resides with ions of energy $\gtrsim 30$ keV. Inside $\sim 40\ R_J$ there appear to be substantial fluctuations in the number density, with a fraction accounted

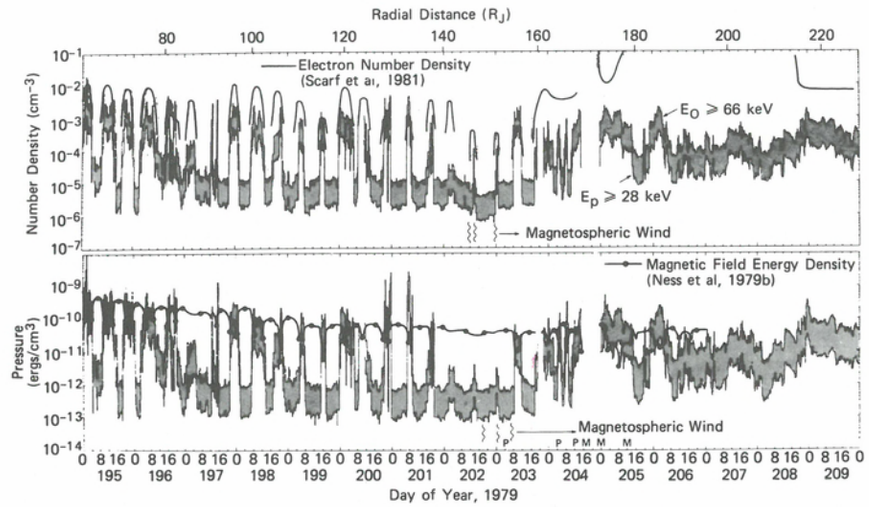

Fig. 4.22. Voyager 2 outbound densities and pressures [Krimigis et al., 1981]. As in the two previous figures, the electron density and magnetic field energy density is given by the solid lines in the upper and lower panels.

for by energetic particles ranging from a few percent to well over 50%, if the assumption is made that the detector response in this region of the magnetosphere is primarily due to oxygen and sulfur.

Figure 4.22 presents data in a format similar to that of Figures 4.18 and 4.19 during the outbound portion of the Voyager 2 trajectory from ~ 70 to $\sim 225\ R_J$. The solid lines are estimated electron concentration profiles from Gurnett et al. [1981b], representing upper limits of the electron concentration during magnetodisc crossings. We note that the measured energetic particle ion densities are typically a factor of 2–5 below the PWS electron densities, although in some cases (for example, early on day 195, late in day 196, middle of day 199, and especially on day 203), the energetic ion densities are in good agreement with the estimated electron density by PWS. The lower panel in the figure shows estimated particle pressures and the corresponding magnetic field energy density. We again observe that the energetic particle pressure in the magnetodisc and the magnetic field pressure in the lobes are similar, as shown by the detailed study of Lanzerotti et al. [1980]. It is important to note that the particle pressure is comparable to the field pressure well outside the boundary of corotational plasma flow (day 203) and into the magnetospheric wind region, up to at least day 206 (i.e., outside the magnetopause).

Anisotropies. The LECP instrument scan plane was optimized to obtain pitch-angle distributions and anisotropies in the outer Jovian magnetosphere as described in Figure 4.2. This was in contrast to the Pioneer spacecraft anisotropy studies, which were primarily obtained in a plane essentially perpendicular to the Jovian equatorial plane and thus were optimized for observing pitch-angle distributions in the inner, dipolar region of the magnetosphere. A standard harmonic analysis was performed using the full 8-sector set of data [Carbary et al., 1981]. The count rate is least-square fit to the function

$$C(\phi) = C_0 [1 + A_1 \cos(\phi - \phi_1) + A_2 \cos 2(\phi - \phi_2)] \qquad (4.15)$$

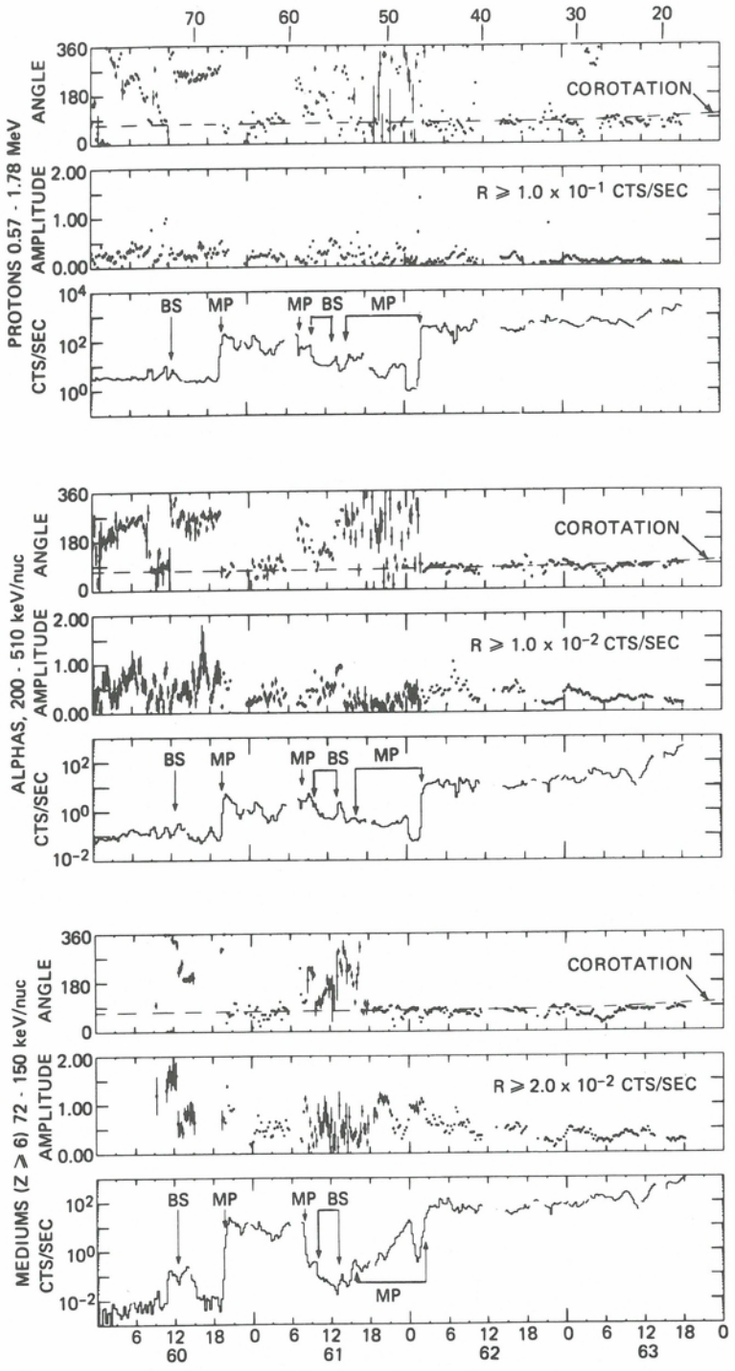

Fig. 4.23. Voyager 1 inbound, detailed anisotropy plots [Carbary et al., 1981]. First order anisotropies for three representative species are shown. Data shown here are 15-min. averages. Bow shock and magnetopause locations are taken from Bridge et al. [1979a] and Ness et al. [1979a].

where C_0 represents a scan average, A_1 is the anisotropy amplitude, and ϕ_1 is the anisotropy angle ($\phi_1 = 0$ represents a flux maximum in sector 8). This analysis will concentrate on the first order (or streaming) anisotropy given by A_1 and ϕ_1. The vector A_1, ϕ_1 defines a flow strength and direction. In a large majority of cases, LECP anisotropies in the Jovian magnetosphere are well described by such a unidirectional fit. To obtain a unique determination of the amplitude, only channels whose response is primarily due to one particle species are used. These are the 0.57–1.78 MeV protons, 0.2–0.5 MeV/nucleon alpha particles, and 0.07–0.15 MeV/nucleon medium nuclei ($Z \geq 6$).

An example of these fits is given in Figure 4.23 that displays anisotropies on the Voyager 1 inbound trajectory. These 15-min. averages reveal a great deal of structure in regions both external and internal to the magnetopause. Anisotropy angles at ~110°–190° represent solar wind flow on day 60. Crossing into the magnetosheath on day 60 after ~1300 UT, LECP measured sheath flows at angles of ~250°. Entry into the magnetosphere on day 60 was signaled by a change in the anisotropy angle from ~260° to ~80°, the latter angle being that of nominal corotation (see also Fig. 4.16). The last magnetopause crossing occurred during a time span of several hours beginning in the latter half of day 61 [Ness et al., 1979a]. Anisotropy angles of protons and alphas were variable during this time interval and so the angle is characteristic of both magnetosheath flow and corotation. However, the $Z \geq 6$ particles have strictly corotational anisotropy directions throughout the series of magnetopause crossings. Within the magnetosphere, anisotropy amplitudes can be variable on timescales of 15 min., although the anisotropy angles of all ion species remained essentially in the sense of corotation (70°–80°). Proton anisotropies are weaker than alpha particle anisotropies, which in turn seem weaker than the $Z \geq 6$ anisotropy; this is expected from the velocity dependence of the convective anisotropy. Except at the magnetopause, the inbound data do not indicate strong spatial gradients in the particle population (scale lengths of ~10 R_J suggested by the rate profiles seem to be appropriate for ions on the dayside). Finally, we note that the anisotropy angles tend to be somewhat less than the nominal corotation angle after the beginning of day 63. This fact is most apparent in the medium Z channel, and is suggestive of a small steady component of radial outflow.

Figure 4.24 displays the Voyager 2 anisotropies within the magnetodisc region from the beginning of day 195 to the end of day 199. The anisotropies reveal a striking correlation with position relative to the midplane of the magnetodisc plasma sheet. The LECP ion anisotropy amplitudes appear to be strongest near the midplane of the plasma sheet and weakest away from the midplane. This effect occurred for all ion species shown. The anisotropy angles do not show similar signs of dependence on distance from the midplane. Generally, the anisotropy angles remained close to the nominal corotation angle (~315°).

The anisotropies of the $Z \geq 6$ particles show the most pronounced effect with radial distance in the region of the magnetodisc. Figure 4.25 shows 1-hr averages of the $Z \geq 6$ particle anisotropies for most of the magnetodisc crossings by Voyager 2. No selective data sorting with distance from the midplane has been done and some of the scatter in the data is probably due to changes in amplitude with Z_{DSC} (i.e., distance from midplane). In spite of the scatter, the anisotropy amplitudes show an easily recognizable linear increase with R. In a more detailed analysis, Carbary et al. [1981] show that the anisotropy amplitude is largest at the equator and decreases as one moves away from the magnetodisc at large values of Z_{DSC}.

Figure 4.26 displays the several days surrounding the Voyager 1 encounter with the wind region. Shown here are low-energy ions with energies 53–85 keV. The space-

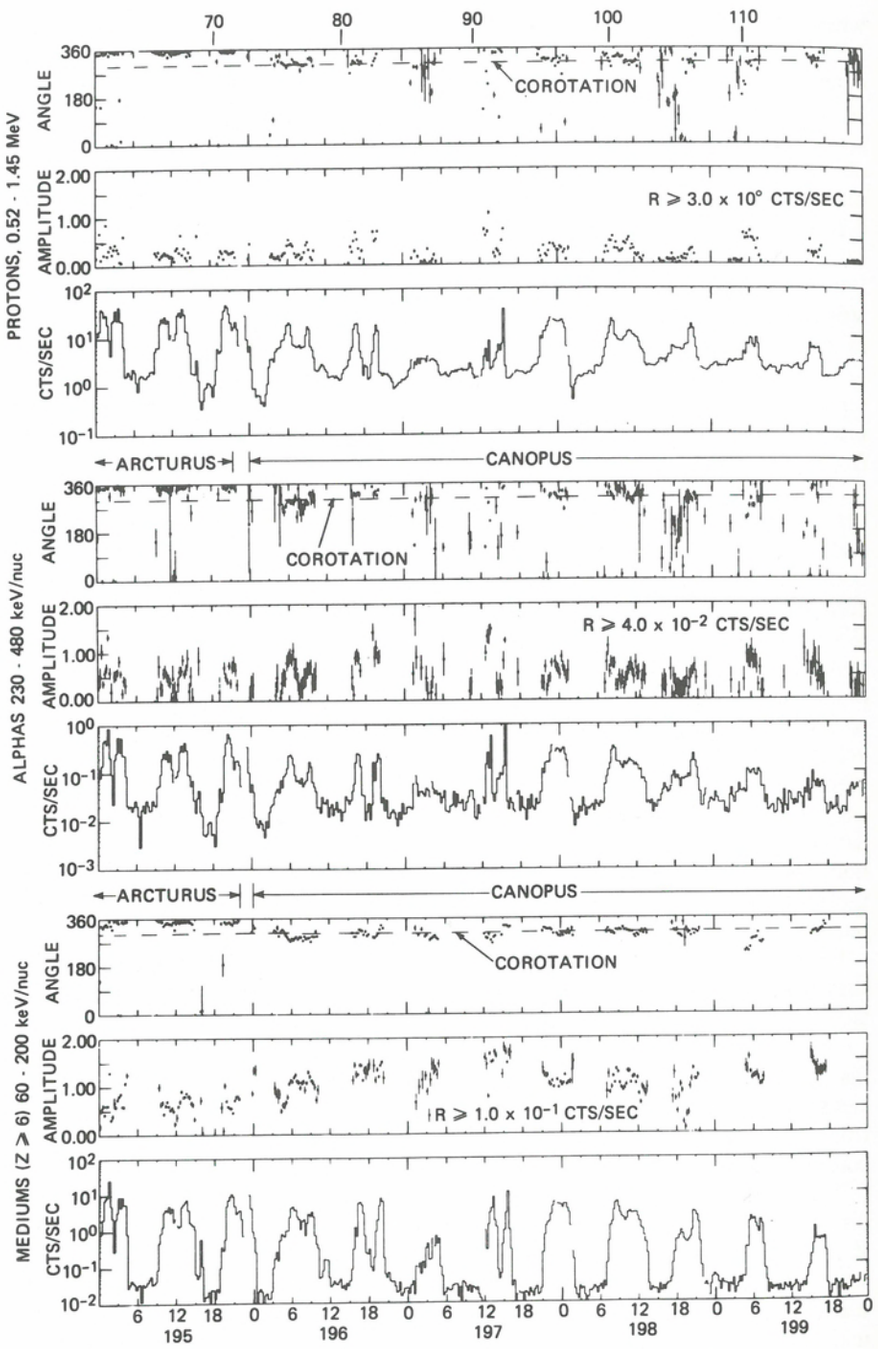

Fig. 4.24. Voyager 2 outbound magnetodisc, detailed anisotropy plots [Carbary et al., 1981]. First order anisotropies are shown in the same format as the previous figure. The data are 15-min. averages. Bow shock and magnetopause locations are taken from Bridge et al. [1979b] and Ness et al. [1979c].

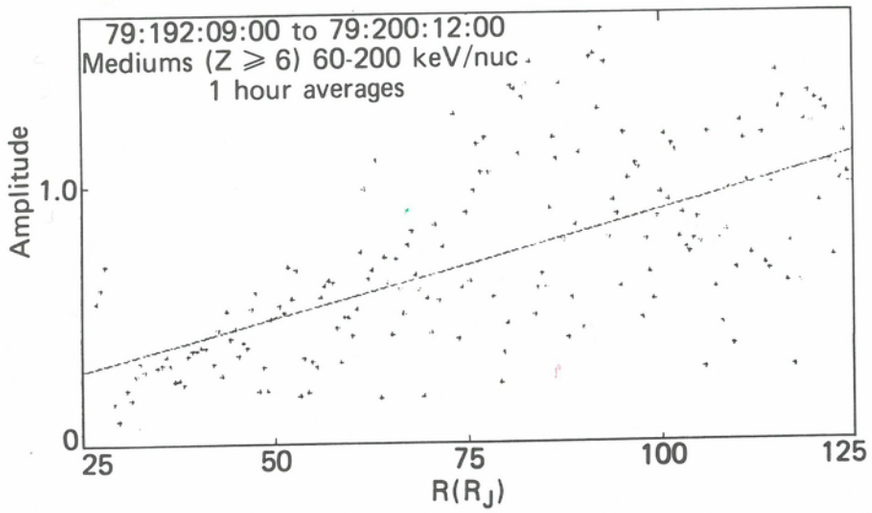

Fig. 4.25. First order anisotropy amplitudes for the medium Z ($Z \geq 6$) particles observed on Voyager 2 outbound [Carbary et al., 1981]. All data points are included, irrespective of spacecraft distance from the magnetodisc. The line represents a least-squares fit to the data.

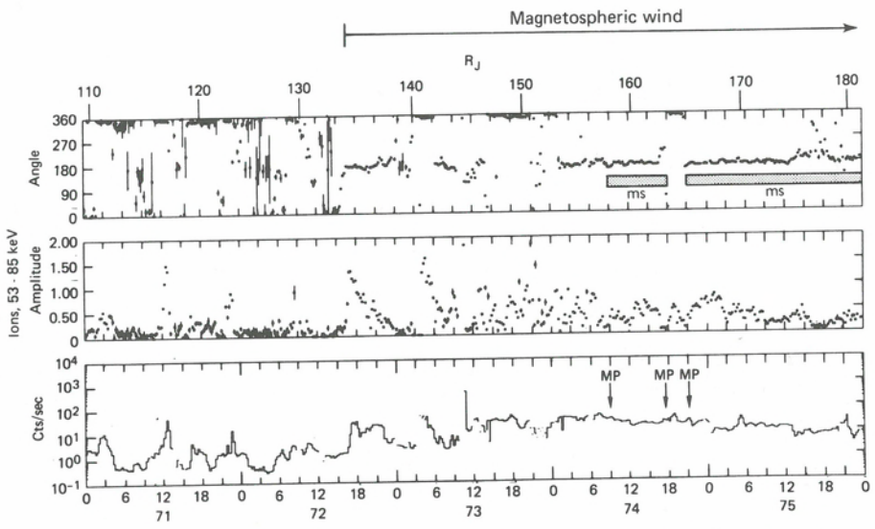

Fig. 4.26. Voyager 1 magnetospheric wind region [Carbary et al., 1981]. The transition from corotational magnetospheric flow (angles near 360° for this orientation) to outward or antisolar flow (angles near 180°) first occurs on day 72, well before the first magnetopause encounter. Magnetopause locations are taken from Bridge et al. [1979a] and Ness et al. [1979a]. The data represent 15-min. averages.

craft's first entry into the wind region occurred near 1200 UT on day 72, ~2 days prior to encounter of the first magnetopause crossing; this can be seen by the abrupt change in the anisotropy angle from ~350° (corotation) to a relatively steady 180° (magnetospheric wind). The 10-hr periodicities associated with the magnetodisc break down in this region (bottom panel), although the anisotropies continue to be very strong. Sudden ~180° changes in the anisotropy angle occurring on day 73 indicate that the

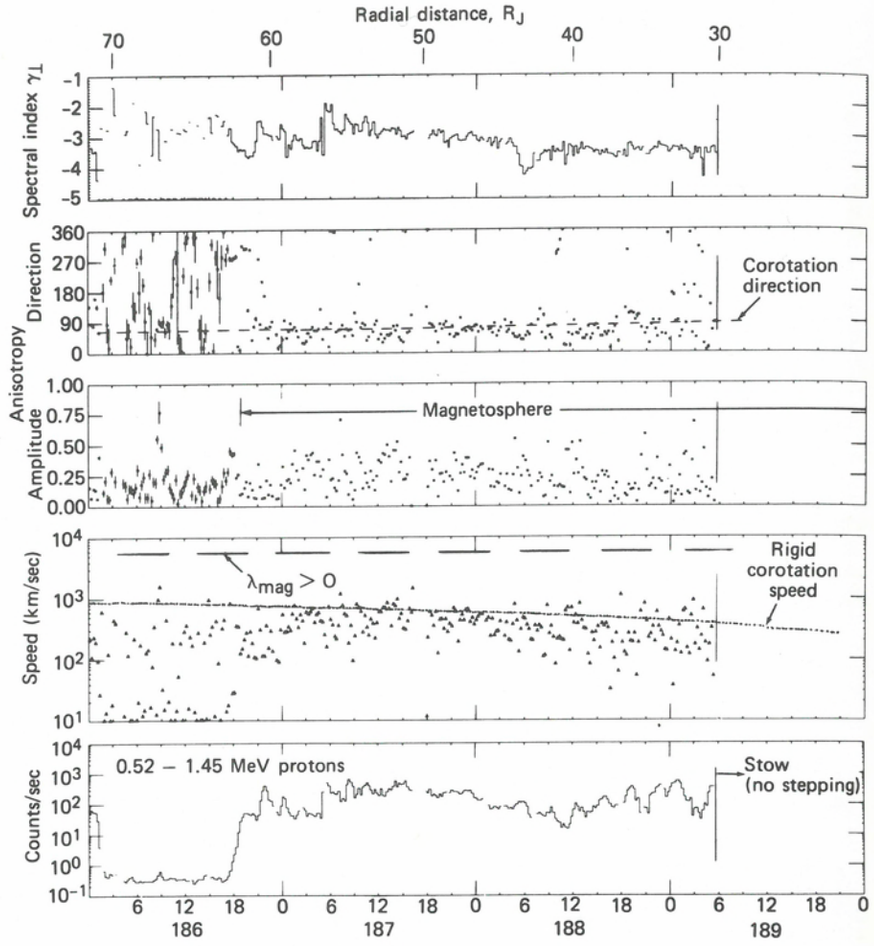

Fig. 4.27. Voyager 2 Compton-Getting speed for 0.57–1.78 MeV protons [Carbary et al., 1981]. The plasma speeds observed during the inbound phase of the encounter are shown in the fourth panel. The corotation speed for a rigid magnetosphere is given by the dotted line. The periods where the spacecraft was in the northern magnetic hemisphere are given by the bar along the top of the panel. The lines in the anisotropy direction panel show the corotation direction. The bar at the top of the anisotropy amplitude panel shows the periods when the spacecraft was inside the Jovian magnetosphere.

disc/wind boundary passed over the spacecraft several times. The spacecraft entered the magnetosheath near the middle of day 74 and reentered the magnetosphere for a short time and again encountered corotational flow. A similar observation was made during the Voyager 2 trajectory, again with the flow vector turning antisunward ~1.5 days prior to the first crossing of the magnetopause. The change from corotational to tailward flow was even more dramatic for Voyager 2 in that it was accompanied by a heavy ion beam described by a relatively cold (~5 keV) Maxwellian with a peak energy at ~265 keV [Krimigis et al., 1980; Krimigis, 1981].

Velocities. Because the convection velocities are much smaller than the velocities of ~1 MeV protons, we can relate the convective speed (V_c) to the particle anisotropy

amplitude (A_1) by the simple rearrangement of Equation (4.8):

$$V_c = \frac{A_1 v}{2(\gamma + 1)} \tag{4.16}$$

We have used Equation (4.16) to compute a radial profile of the convection speeds in the dayside Jovian magnetosphere. A_1 is the measured first order Compton-Getting anisotropy amplitude as defined in Equation (4.8), where γ is the observed spectral index (for 0.5–4 MeV protons) perpendicular to corotation [Krimigis et al., 1981], and v is determined from the mean energy of the proton channel used. Figure 4.27 shows the speeds derived from Equation (4.16) during the inbound portion of the Voyager 2 encounter using the indicated proton channel. The time profile of the count rate and computed speed are shown in the lower two panels whereas the corresponding anisotropy amplitude, phase, and spectral index are shown in the upper three panels. The dotted curve in the fourth panel indicates the speed corresponding to a rigidly corotating magnetosphere, although the dashed line in the second panel indicates the expected corotation direction. It is evident from the speed profile that velocities are close to that of corotation in the outer part of the magnetosphere but exhibit considerable structure especially toward the inner magnetosphere. The corresponding Voyager 1 profile (Chap. 5) shows (~10 hr) variation in the speed inside ~50 R_J. In agreement with the speed profile of McNutt et al. [1979], the LECP speeds are consistently less than corotation within ~20 R_J of Jupiter. It should be emphasized that even though individual measurements of anisotropy angles often depart significantly from the corotational direction, the flow orientation is generally near the corotation direction.

Velocities in the nightside magnetodisc are not as readily obtainable, primarily due to unfavorable orientation of the LECP scan plane with respect to the corotation direction. In those cases where the orientation was favorable, it has been determined [Lanzerotti et al., 1980] that convective speeds are well below corotation for radial distances beyond ~80 R_J. Using similar techniques, it has been determined that velocities in the magnetospheric wind region are in the range of 300–900 km s^{-1}.

Composition and charge states. The most unusual aspect of the Voyager 1 and 2 encounters with Jupiter in terms of energetic particles was undoubtedly the composition. As shown in Section 4.2, the composition of magnetospheric particles is primarily made up of He, S, and O in addition to protons, with a small percentage of Na. The Pioneer encounters in 1973 and 1974 gave no hint that such composition might exist in the magnetosphere primarily because the instruments were not optimized to make measurements in the appropriate energy range. As noted in Figure 4.8*c*, there are important changes in the abundance ratios as functions of radial distance, that can be used to infer sources and/or acceleration mechanisms. Similar variations of the relative abundances are also observed in the magnetodisc and the magnetospheric wind regions.

Figure 4.28 shows selected abundance ratios during the Voyager 2 outbound pass out to ~200 R_J. The data from 10–60 R_J in Figure 4.8*c* are repeated, but in a slightly different format with the lower three panels showing the variation of various elements with respect to oxygen. Beyond ~60 R_J, all ratios show departures from their values in the middle magnetosphere to values that are more typical of solar particles. Another qualitative change in the ratios occurs at ~160 R_J. This is approximately the point at which the anisotropy of the lower energy ions switched from being predominantly in the corotation direction to being directed away from Jupiter, forming the magnetospheric wind. The transition occurred before the first magnetopause crossing that is

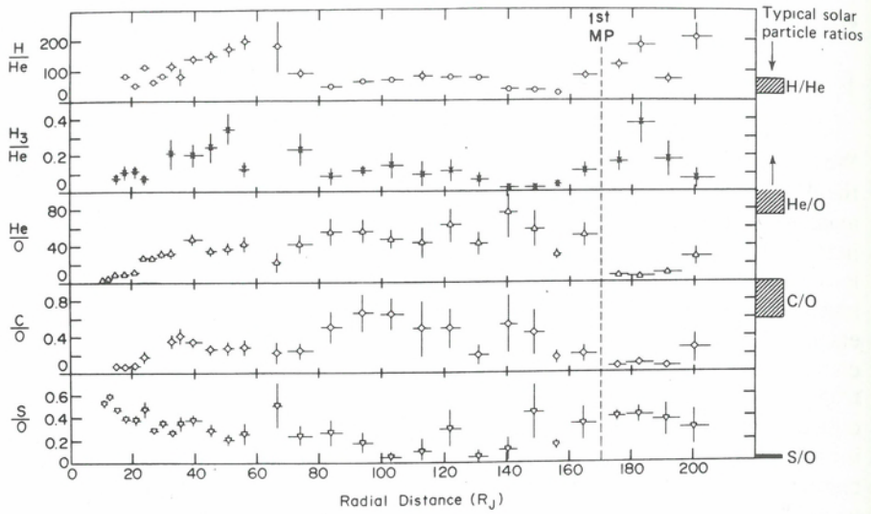

Fig. 4.28. Selected abundance ratios from 10–200 R_J during the outbound pass of Voyager 2 [Hamilton et al., 1981]. Between 43 and 160 R_J, the ratios were calculated only for periods near the current sheet. The first of several magnetopause crossings is indicated at ~170 R_J. Voyager 2 entered the magnetospheric wind region at between 160 and 170 R_J. Solar abundances of the ratio are noted on the right-hand ordinate.

indicated in Figure 4.28, and was apparently not affected by several other magnetopause crossings detected between ~170–185 R_J [Bridge et al., 1979*b*].

In the wind region, the abundance ratios at ~1 MeV/nucleon ions can be described as being more Jovian than solar in nature. S, O, H_3^+, and H abundances are all high relative to C and He. From Figure 4.6, we see that the energetic particle intensities were also higher in the wind region than in most of the magnetotail. Hamilton et al. [1981] note that even beyond 200 R_J there were instances when the composition of heavy ions was more similar to that in the inner magnetosphere than to that characteristic of solar/interplanetary particles. The overall impression from Figure 4.28 is that although the magnetodisc may be relatively poor in terms of heavy ions [see also Lanzerotti et al., 1980], the magnetospheric wind exhibits a distinctly Jovian composition suggesting that most of the flux comes from the inner part of the Jovian magnetosphere.

The changes in the relative abundance ratios are crucially dependent on the form of the energy spectrum; changes in the ratios with location or time could reflect either changes in the relative densities of the various species or only the relative changes in spectral slopes or both. The obvious question is whether there exists a representation where the spectra of all particle species are identical so that the relative abundances actually reflect the concentrations of the elements in the source plasma.

To investigate the spectral dependence noted above, a set of spectra for the various species in the outer magnetosphere is presented in Figure 4.29*a*. As is evident from the figure, all species have different slopes so that the relative abundances depend on the energy at which the ratios are evaluated. Hamilton et al. [1981] have shown that the most appropriate representation of the spectra in Jupiter's magnetosphere is on the basis of energy/charge. Their result is shown in Figure 4.29*b* which uses the identical data as those presented in Figure 4.29*a*, and also extends the energy range to lower

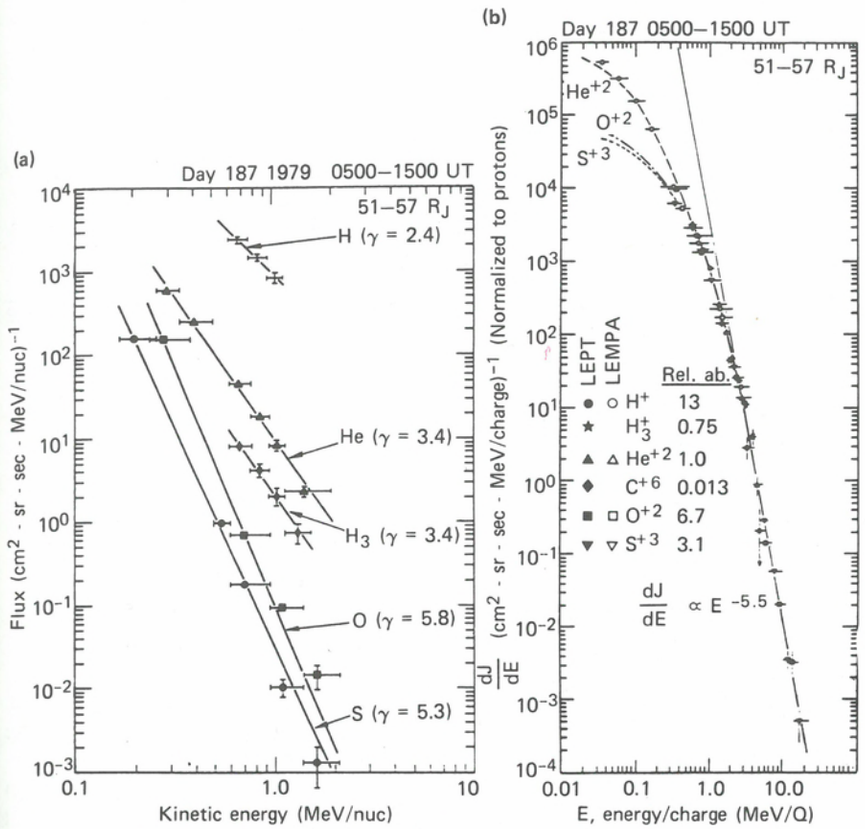

Fig. 4.29. (*a*) Energy spectrum of the indicated species plotted versus energy per nucleon (equal velocity); (*b*) differential intensities of the same species but plotted as a function of energy per charge [from Hamilton et al., 1981].

energies where the species are not identified uniquely. Here the intensities have been evaluated at a given energy/charge and the curves representing each element were displaced vertically by a factor indicated in the figure as "relative abundances." A charge state of +2 was assumed for oxygen and +3 for sulfur, primarily based on the charge states inferred from the UV experiment data [Broadfoot et al., 1979]. It is evident that in this representation, the energy spectra of all species fit on a common curve, and the relative displacements form the basis for estimating the relative number densities for all species. We note from the relative abundances that the number of $Z \geq 2$ ions is comparable to the number of protons. Thus, by inference from the energetic ions, the Jovian plasma is unique among magnetospheric plasmas in that it is dominated by ions heavier than hydrogen (see also Chap. 3).

Hamilton et al. [1981] have also demonstrated that the energy per charge representation is most appropriate for the entire magnetosphere and the magnetospheric wind region. In this representation, the large increases in the flux ratios of oxygen and sulfur relative to helium at equal energy/nucleon between the outer and inner magnetosphere (Figure 4.8*c*) are in fact consistent with flux ratios of ~1 at equal energy/charge, with no change in the value of this ratio with radial distance. The same procedure applied to the H/He ratio at equal energy/charge gives a roughly constant value of ~15. By

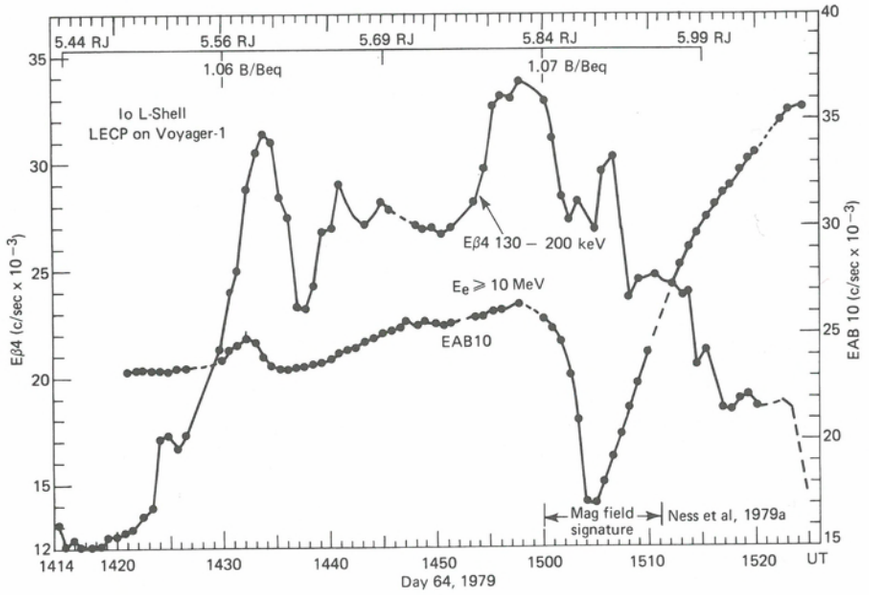

Fig. 4.30. Low and high energy electron profiles during close encounter of Io. Points are 48-s averages; missing data are indicated by dashed lines.

formalizing the procedure of expressing the energy spectra in terms of energy/charge, Hamilton et al. [1981] were able to parametrize the problem and deduce the charge state of heavier ions as follows: C^{+6}, $O^{+2,+3}$, and $S^{+3,+4}$. Thus, the energy/charge representation not only removes the radial dependence of the abundance ratios shown in Figure 4.8*c*, but enables the deduction of the relative charge states of all the ions and results in relative abundances that probably reflect those of the source plasma (see also Chap. 3).

Inner magnetosphere

The LECP instrument obtained a large number of measurements in the inner magnetosphere as well, some of which have been reported by Krimigis et al. [1979a], Armstrong et al. [1981], and Lanzerotti et al. [1981] (see also Chap. 12). The significance of these measurements lie primarily in the extended energy spectra and species coverage, and their relationship to the location of the Io plasma torus. These measurements complement and extend the measurements obtained by the Pioneer spacecraft, and their significance and implications are discussed in other chapters (Chaps. 5, 8, and especially 12). The original material may be found in the references cited above.

One particular aspect of the inner magnetosphere passage of Voyager 1 is worthy of note, namely the close approach to Io. During this passage only the energetic (> 10 MeV) electron fluxes show definite evidence of an interaction of the particles with field lines that may have passed through Io [Krimigis et al., 1979a]. A detailed plot of the intensity of low and high energy electrons in the vicinity of Io's *L*-shell is shown in Figure 4.30. Here, we note that the high energy electrons decreased by approximately 30% at the same time as a perturbation in the local magnetic field was observed [Ness et al., 1979a]. However, no significant change specifically associated with the magnetic field signature is clearly observed in the low energy electrons. These electrons

display an overall enhancement in association with the Io flux tube, reminiscent of the electron "spike" observed by Fillius [1976] during the Pioneer 10 passage through the Io *L*-shell. Additional analysis is necessary before this increase in intensity can be ascribed to acceleration processes expected to take place in the vicinity of Io. It must be noted, however, that increases of this magnitude or larger in the intensities of low energy electrons have been seen throughout the inner magnetosphere passage [Krimigis et al., 1979a; also Fig. 12.3]. The possibility exists that after analysis of the full data set an upper limit to a possible magnetic moment associated with Io could be made [Krimigis et al., 1979a; Southwood et al., 1980; Ip, 1981; Kivelson and Southwood, 1981].

4.5. Recapitulation and open questions

We now review those properties of the magnetosphere environment that were established by the observations (Secs. 4.2 and 4.4) and identify areas where open questions still exist. We find it helpful to view the results in the context of the model presented in the summary Figure 4.4.

It has been established that most of the plasma in the outer magnetosphere is hot (~ 20 to 40 keV), and that it more-or-less corotates with the planet all the way to the magnetopause on the dayside; on the nightside, the hot plasma suddenly breaks into an antisunward flow inside the magnetopause at a distance from ~ 130 to ~ 160 R_J, which continues to large distances past the downstream bow shock. Further, the plasma is hotter at the magnetic equator than off it.

The ion energy spectrum ($\gtrsim 30$ keV) is characterized by a thermal part described well by a convected Maxwellian, and a nonthermal component that can be fit by a power law in energy, with the transition point between the two components at ~ 150 to 250 keV. The composition of the nonthermal component is primarily H, He, O, and S. This composition is also consistent with the angular distributions measured at lower (< 200 keV) energies. In fact, by expressing the spectra in terms of energy/charge all particle species display identical spectral forms, suggesting an electric field acceleration process. Using this procedure, it is possible to deduce the relative densities and charge states of the source plasma: O^{+2}, S^{+3}, C^{+6}, and relative densities of hydrogen to heavier ($A > 1$) ions of ~ 1:1. Finally, the electron spectrum below ~ 200 keV displays a thermal distribution not unlike that of the ions.

The energetic ions ($E \gtrsim 30$ keV) appear to dominate the plasma pressure inward to at least ~ 10 R_J and they thus determine the statics and dynamics of the magnetosphere. These ions are responsible for the inflation of the dayside magnetosphere to about twice the distance expected on the basis of the observed dipole magnetic moment. This interaction with the solar wind is different from that at Earth or any of the planets investigated so far. Because of the high-beta plasma (thermal energy density exceeding magnetic energy density), we expect that the shape of the magnetopause is not likely to be smooth and could exhibit "bulges" owing to variations between solar wind and Jovian plasma pressure. There is evidence from low-energy ion streaming events that Jovian plasma escapes frequently into the upstream and downstream solar-wind regions.

It was theoretically expected even before the Pioneer flyby [Ioannidis and Brice, 1971] that the transport of ionospheric plasma in the Jovian magnetosphere might be predominantly outward, in contrast to the Earth where it is predominantly inward. Mestel [1968] pointed out that a cold plasma can break out into radially outflowing wind when the corotational energy density approximates the magnetic energy density at the critical point of the flow (Alfvén radius). Michel and Sturrock [1974] proposed

that the Jovian internal plasma sources would centrifugally drive a "planetary wind" similar to the solar wind. This idea was expanded on by Coroniti and Kennel [1977] and Kennel and Coroniti [1977b] who retained the features of an axially symmetric outflow interacting with the solar wind. Hill, Dessler, and Michel [1974] took the view that the solar wind would block the outflow on the dayside and the wind would only flow out the tail.

The observations have brought out a number of serious contradictions to these early expectations. The basis for the models is that the opening distance occurs when the cold (ionospheric) plasma corotational energy density equals the magnetic field energy density, resulting in pre-Voyager predictions for the opening radius from ~ 30 to $\sim 70\ R_J$. Using the actually observed cold plasma densities and composition at Io (Chap. 3) in these models, reduces the opening distance to $\sim 10\ R_J$ [see, for example, discussion in Kennel and Coroniti, 1979]. The distance where plasma outflow begins was observed by Voyager to be in the range of ~ 130 to $\sim 160\ R_J$ on the nightside; some evidence exists that there is magnetospheric plasma escape upstream of Jupiter as well (see Fig. 4.3). In addition, all theories assumed the plasma to be cold at the opening radius, but the observations give temperatures of ~ 30 keV. Finally, the models assumed initially that the plasma source is the ionosphere, rather than the satellites. The observations also show (see Fig. 4.28) that the composition in the wind is similar to that of the magnetosphere inside $\sim 30\ R_J$, rather than the magnetodisc, as the models suggest. For these reasons, the plasma outflow discovered by Voyager was named "magnetospheric wind" [Krimigis et al., 1979b] rather than planetary wind. It is evident that the wind phenomenon modeled for the magnetosphere of Jupiter by a direct application of Mestel's [1968] stellar wind concept does not correspond to the Voyager findings. The early theoretical models, although valuable in expanding our perspective, need to be reviewed critically, in view of the observations (see Chaps. 10 and 11 for additional discussion).

The magnetospheric wind apparently represents the principal loss process of hot plasma from the magnetosphere. Krimigis et al. [1981] estimate the ion loss rate at $\sim 2 \times 10^{27}\ s^{-1}$ and the energy loss rate at $\sim 2 \times 10^{13}$ W. These compare with supply rates of $\sim 3 \times 10^{28}\ s^{-1}$ (dominated by Io and, in the case of protons, by Jupiter), and $\sim 10^{15}$ W (dominated by Jupiter) [Krimigis et al., 1981; Chap. 10].

Despite the overall consistency of the results and interpretations, we must keep in mind that our conclusions are of necessity based on only the all too brief Pioneer and Voyager flybys through a small part of a very large, heterogeneous and dynamic magnetosphere. Some of the results are probably more valid than others. For example, the hot plasma is probably characteristic of the magnetosphere at all local times, as is the rather exotic composition. The magnetospheric wind region, on the other hand, has only been sampled twice in the ~ 0300 to 0500 local time regions, and could be drastically different at other parts of the nightside magnetosphere, such as local midnight or dusk. It is unlikely that the plasma circulation pattern on the nightside is as simple as has been drawn in Figure 4.4.

There exist other areas of uncertainty, some of which will probably be addressed by more detailed studies of the combined Voyager data sets, whereas others must await the more definitive measurements to be obtained by the Galileo spacecraft such as the spectral region between the PLS and LECP measurements (~ 6 to ~ 28 keV for ions, and ~ 6 to ~ 14 keV for electrons), although no major surprises should be expected there. It is likely that the temperature and number density of the plasma are highly variable, and there may be substantial variations in the relative concentrations of the hot and cold components. Three-dimensional flux measurements should help illuminate the overall circulation pattern, which could only be inferred indirectly by the Voyager

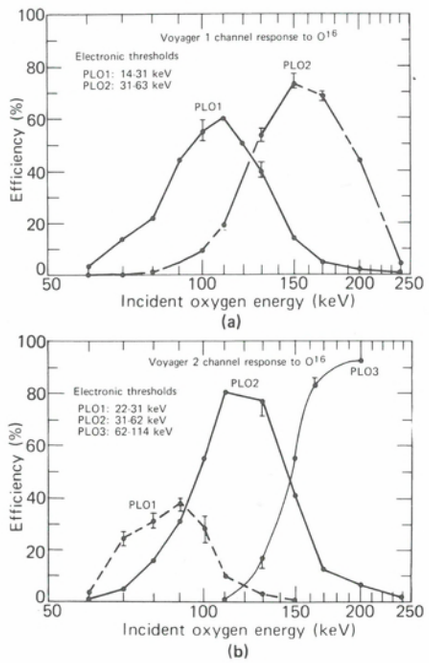

Fig. 4.31. Efficiency functions for the detection of ^{16}O nuclei in the Voyager 1 and 2 LEMPA detectors [Krimigis et al., 1981]. The reduced efficiencies for the PL01 and PL02 channels are a result of the relatively large FWHM of the deposited energy in the detector (~ 16 keV) compared to the width of the channels.

measurements. We certainly hope that, as the data analysis proceeds, additional features of essential significance to the physics of the Jovian magnetosphere will emerge that will allow the construction of more sophisticated models, the predictions of which can be checked by future spacecraft or ground-based observations.

APPENDIX A: INSTRUMENT RESPONSE

For all ion channels of LEMPA, a sufficiently accurate expression for the contribution from ion species "a" to the rate $R_k^a(\mathbf{n})$ of the k^{th} energy channel when the detector looks in the direction of the unit vector $\mathbf{n}$ is

$$R_k^a(\mathbf{n}) = G \int_0^\infty dE\, \epsilon_k^a(E)\, j^a(E, -\mathbf{n}) \tag{4.17}$$

where $j^a(E, \hat{\mathbf{p}})$ is the incident undirectional differential particle flux for species "a", and $\epsilon_k^a(E)$ is the detector efficiency function for the k^{th} energy passband, averaged over the detector area $\Delta\sigma$ and solid angle $\Delta\omega$. The "geometric factor" G is the integral of $|\hat{\mathbf{p}} \cdot \mathbf{n}|$ over the same area $\Delta\sigma$ and solid angle $\Delta\omega$. Efficiency curves $\epsilon_k^a(E)$ for the response to ^{16}O in the lowest ion channels on Voyagers 1 and 2 are shown in Figure 4.31 and additional response curves for ^4He, ^{32}S, and ^{40}Ar may be found in Krimigis et al. [1981]. For very steep or highly peaked spectra, the energy dependence of the channel efficiencies is an important consideration, and the use of a "band-passed" efficiency $\bar{\epsilon}_k^a$ in order to write

$$R_k^a \simeq G\, \bar{\epsilon}_k^a\, j_k^a\, \Delta E_k^a \tag{4.18}$$

where j_k^a is the differential flux centered within an appropriately chosen channel passband ΔE_k^a, must be considered a rough approximation. These approximate channel passbands for the LEMPA may be deduced from curves such as shown for ^{16}O in Figure 4.31.

Of course – and here is our main challenge – the rate of k^{th} channel is due to the sum of the rates produced by all the species present, so the measured quantity is the rate

$$R_k(\mathbf{n}) = G \sum_a \int_0^\infty dE\, \epsilon_k^a(E)\, j^a(E, -\mathbf{n}) \tag{4.19}$$

APPENDIX B: IMPROVED SPECTRAL MODELS

When calculating the contribution of a given ion species to a particular energy channel, the most useful quantity is the integral flux $J(E,\phi)$ above an energy E in the scan direction ϕ (because the incident flux in a finite energy band with uniform efficiency can be deduced from this function). For a convected thermal spectrum, it is easily seen from the formulas (4.11) and (4.12) that $J(E,\phi) = N_v F(kT/E, V/v, \phi)$, where N is the density of thermal density and v is the particle speed corresponding to energy E. The function F is then a "universal" function of only the dimensionless ratios kT/E (thermal energy normalized by particle energy) and V/v (bulk velocity normalized by particle velocity). Consequently only a single computation of the universal function F over its three dimensionless variables is required for a theoretical estimate of the directional integral flux due to streaming ions with a Maxwellian distribution. For any particular species, energy, temperature, and bulk velocity, one simply evaluates the dimensionless variables kT/E and V/v to obtain the integral flux $J = NvF$.

The universal function $F(x,y,\phi)$ is presented in Figure 4.32*a* as a logarithmic contour plot for $\phi = 0$ and $\phi = \pi/2$ (integral fluxes parallel and transverse to the flow direction). The contours reveal the extreme "front-to-side" anisotropy ratios $J(E,O)/J(E,\pi/2)$ expected from a convected Maxwellian for $kT/E \lesssim 1$ and $V/v \lesssim 0.1$, that is, particle energies well above the thermal energy and particle velocities approaching the order of the bulk velocity. This suggests that the particle anisotropy would be strongly affected by any nonthermal tail on the energy spectrum, particularly in the directions $\phi \gtrsim 90°$ for $E > kT$ and $v \sim V$.

Nonthermal tails in plasma accelerated from substrate thermal distributions are apparently intrinsic to ion acceleration processes upstream of the Earth's bow shock [Lin, Meng, and Anderson, 1974], in the Earth's magnetotail [Sarris, Krimigis, and Armstrong, 1976], on the Sun [Zwickl et al., 1978], and in corotating shock structures in the solar wind [Gloeckler, Hovestadt, and Fisk, 1979; Gosling et al., 1981]. They are also evident in the Jovian ion spectra presented by Krimigis et al. [1979a,b], as can be seen from Figures 4.9 and 4.14. Consequently, when analyzing the LEMPA measurements of convective plasma in the magnetodisc, we face the compound problem of an unknown spectral form and an unknown ion composition.

Therefore we developed a model spectrum incorporating a very simple parametrization of a nonthermal tail called a "γ-thermal" distribution which has been applied successfully to flowing plasma in the earth's magnetosphere by Sarris et. al., 1981. In the plasma frame, we set the differential flux $\tilde{j} \propto \tilde{E} \exp(-\tilde{E}/kT)$ for $\tilde{E} \le E_1$, and $\tilde{j} \propto (\tilde{E}/E_1)^{-\gamma}$ for $\tilde{E} \ge E_1$, where $\gamma + 1 = E_1/kT$. This spectrum makes the transition from a

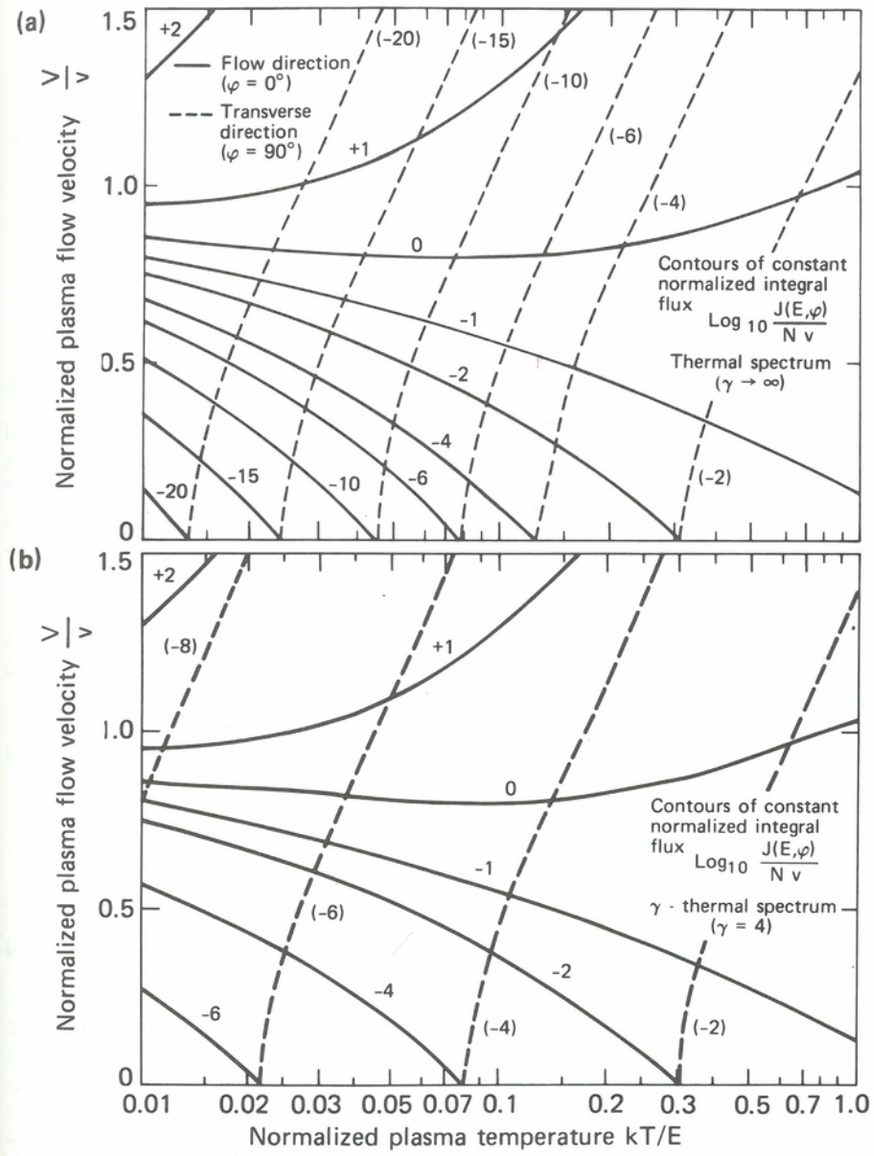

Fig. 4.32. (*a*) Logarithmic contours of integral particle flux of convected thermal particles J normalized by N_v (total density times velocity), as a function of temperature (kT) normalized by particle energy (E), and convection velocity (V) normalized by particle velocity (v). Solid line contours are for integral ion fluxes parallel to convection ($\phi = 0$), and dashed are for those transverse to convection ($\phi = \pi/2$). The front-to-side ratio $J(E,O)/J(E, \pi/2)$ may be read off at intersection of solid and dashed curves. (*b*) Same representation as (*a*), but for a "gamma-thermal" spectrum ($\gamma = 4$), such as shown in Figure 4.33.

Maxwellian to a power law in the plasma frame at energy $\tilde{E} = E_1 = (\gamma + 1)\,kT$ with no discontinuity in intensity or slope. Several sample spectra are shown in Figure 4.33 and should be compared with observed spectra which can be fit with the γ-thermal form, as

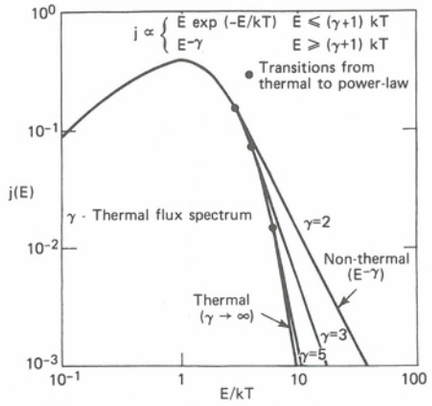

Fig. 4.33. The "γ-thermal" model differential flux spectrum, which makes a continuous transition from a thermal distribution with temperature T to a nonthermal tail described by a power law $E^{-\gamma}$ at energy $E = (\gamma + 1)\,kT$.

shown in Figures 4.9 and 4.14. This functional form has significant computational advantages over other functions (such as the "kappa" distribution), when comparison with energetic particle measurements is required. One can still define a "universal" function $F(x,y,\phi,\gamma) = J(E,\phi,\gamma)/Nv$ with $x = kT/E$ and $y = V/v$, but F now depends on γ as well. The effect of the nonthermal tail on an integral flux plot like that of Figure 4.32*a* (one of which can be done for each value of γ), is to shift drastically the positions of the contours in the lower left-hand corner of the plot ($kT/E < 0.1$, $V/v > 0.7$). For example, we show in Figure 4.32*b* a logarithmic plot for the universal function $F(x,y,\phi,\gamma)$ with $\gamma = 4$. Comparing with Figure 4.32*a*, the contour $J/Nv = 10^{-20}$ in the extreme corner of the thermal plot becomes $J/Nv = 10^{-7}$ for the γ-thermal distribution. This parametrization is quite useful for the LECP instrument, because the power-law indices are readily determined from the higher energy LEPT channels where protons, alphas, and medium nuclei are separately identified.

APPENDIX C: MEASUREMENT OF DENSITY AND PRESSURE IN THE PRESENCE OF CONVECTION

The composition of the hot Jovian plasma is one of the most interesting of the scientific questions raised by the LECP observations. However, it is precisely the composition that must be assumed for any mathematical modeling of the LEMPA response. Consequently, an alternative, but complementary approach was taken where lower bounds on density (N), pressure (P), and convection velocity (V) could be obtained from the general properties of distribution functions summarized by (4.3) and (4.4) without invoking parametrized models.

Density. By definition, the density of species "a" is

$$N^a = \int d^3\,p f^a = \int_0^\infty \frac{dE}{v} \int_{4\pi} d^2\omega j^a(E,\hat{\mathbf{p}}) \tag{4.20}$$

This looks tantalizingly like (4.19), except for the inverse power of v that occurs in (4.20) but not in (4.19). This factor causes real difficulty, because, when we try to sum

(4.20) over species to get the total density, v is smaller (for a given energy) for the heavier ions. Also, (4.20) involves fluxes in all directions whereas our rates are only measured in the scan plane. In strong convective flows, the anisotropies may be quite strong (particularly, as we shall see, for the heavy-ion species). However, if the scan-plane measurements happen to contain the direction of convective flow, these usually provide sufficient information to reconstruct the omnidirectional average needed for (4.20). Let us therefore introduce into (4.19) a "scaling velocity" v_k for the k^{th} channel to try to handle the troublesome factor of v. We then form the sum

$$\sum_k \sum_{\mathbf{n}} \frac{2\pi\Delta\mu_n}{G v_k} R_k(\mathbf{n}) = \sum_a \int_0^\infty \frac{dE}{v} \sum_{\mathbf{n}} \frac{2\pi\Delta\mu_n}{G} \left[\sum_k \frac{v}{v_k} \epsilon_k^a(E) \right] j^a(E,-\mathbf{n}) \tag{4.21}$$

By $\sum_{\mathbf{n}}$ we mean the sum over the sector orientations $\mathbf{n}$ of the detector scanning in azumith, and $2\pi\,\Delta\mu_n$ is the representative solid angle assigned to the detector in the n^{th} position, $\theta = 0$ being assigned to the direction in the scan plane closest to the convection velocity (i.e., within the peak sector).

Comparison of (4.20), summed over all species, with (4.21) reveals that if we chose the v_k such that, for all energy ranges of the dominant species over which $j^a(E)$ makes a significant contribution to the energy integral,

$$\sum_k \epsilon_k^a(E) \frac{v}{v_k} < 1 \quad \text{(dominant "}a\text{")} \tag{4.22}$$

then we obtain a lower bound on the density from (4.21)

$$N > \sum_{\mathbf{n}} \sum_k \frac{2\pi\Delta\mu_n}{G v_k} R_k(\mathbf{n}) \tag{4.23}$$

The inequality (4.22) can be satisfied trivially by choosing a sufficiently large v_k, but the larger the value of v_k, the less information there is in the lower bound given by (4.23). Also, reference to Figure 4.31 reveals the importance of the channel efficiency functions ϵ_k^a in identifying the dominant species in a given channel. Krimigis et al. [1979] used a form close to (4.23) that replaced the weighted sum over $\mathbf{n}$ by 4π times the scan averaged rates for each channel. By using v_k as the velocity of protons at the center of each energy band, they argued that they obtained a lower bound on N because the protons had the highest velocity among the expected dominant species present in the outer magnetosphere (see Sec. 4.4 and Figs. 4.20, 4.21, and 4.22).

These same authors also argued that an upper bound on the density could similarly be obtained from the RHS of (4.23) by choosing the v_k to be the midchannel ^{16}O velocity, assuming that this low velocity would reverse the inequality. This procedure will yield a good upper bound only if there are no significant fluxes of ions at energies below the LEMPA ion channel passbands because these would contribute to N^a in (4.20) but would not appear in (4.23). However, it was the lower bound (4.23), as it was evaluated by Krimigis et al. [1979b] with v_k chosen for ^1H, which demonstrated that the bulk of the hot magnetodisc plasma is in the tens of keV temperature range (see Sec. 4.4).

Pressure. There is another approach that leads to an independent estimate of density, but more importantly, to an estimate of pressure which is minimally affected by the strong anisotropies produced by the presence of substantial numbers of heavy ions. Figure 4.11*b* suggests, intuitively, that j^a and $\tilde{j}^a$ should be roughly comparable when the detector direction $\mathbf{n}$ is transverse to the convection velocity. Examination of the figure shows that this approximation will underestimate the contributions of the heavier ions, but we are interested only in a lower bound on the pressure. If we write $\mathbf{v} \cdot \mathbf{V} = vV\cos\theta$, then for $\theta = \pi/2$, $\tilde{v}^2 = v^2 + V^2$ and $\tilde{\theta} = \tan^{-1} v/V$. Thus, a transverse measurement of j^a is related to $\tilde{j}^a$ evaluated at a higher energy $\tilde{E} = (m_a/2)(v^2 + V^2)$ and at an angle $\tilde{\theta}$ different from $\pi/2$. The ratio of the energies is $\tilde{E}/E = 1 + V^2/v^2$, and this is near unity if $V << v$, in which case $\tilde{\theta} \simeq \pi/2 + V/v$. If we have reason to believe that the flux $\tilde{j}^a$ is not strongly anisotropic in the plasma frame, this permits the use of the transverse flux to estimate density and pressure in that frame [Lanzerotti et al., 1980].

First, we write the expression for the average scalar pressure, $\tilde{P}^a$, which must be computed in the frame where the bulk velocity $\mathbf{V}^a = 0$ [Spitzer, 1962]:

$$\tilde{P}^a = \frac{m_a}{3} \int_0^\infty d\tilde{E}\, \tilde{v} \int_{4\pi} d^2\tilde{\omega}\, \tilde{j}^a(\tilde{E}, \tilde{\mathbf{p}}) \tag{4.24}$$

Applying the transformation (4.4) for the transverse direction $\hat{\mathbf{p}} = (-\mathbf{n}_\perp)$ gives

$$\tilde{j}^a(\tilde{E}, \tilde{\mathbf{p}})\tilde{v} = \left(1 + \frac{V_a^2}{v^2}\right)^{3/2} j^a(E, -\mathbf{n}_\perp)v \tag{4.25}$$

By fixing the direction $\hat{\mathbf{p}} = -\mathbf{n}_\perp$, the vector $\tilde{\mathbf{p}}$ becomes a function of $\mathbf{E}$ through the transformation $\tilde{\mathbf{p}} = -m_a(\mathbf{n}_\perp v + \mathbf{V}_a)$. However, in the approximation that $\tilde{j}^a$ is nearly isotropic, this $\tilde{\mathbf{p}}$ dependence has little effect; otherwise it would greatly increase the complexity of the calculation. From the energy transformation $\tilde{E} = E + m_a V_a^2/2$ we have $d\tilde{E} = dE$, so the range of integration $0 < E < \infty$ corresponds to $m_a V_a^2/2 < \tilde{E} < \infty$ because particles with $\mathbf{v} = (-\mathbf{n}_\perp)v \to 0$ in the spacecraft frame still have $\tilde{\mathbf{v}} \to -\mathbf{V}_a \neq 0$ in the plasma frame. Consequently a detector looking in the transverse direction in the spacecraft frame is not responding to energies $\tilde{E} < E_a = m_a V_a^2/2$ in the plasma frame. Thus, under the weak-anisotropy approximation $\tilde{j}^a(\tilde{E}, \tilde{\mathbf{p}}) \simeq \tilde{j}^a(\tilde{E})$.

$$\bar{P}^a = \frac{4\pi m_a}{3} \int_0^{E_a} d\tilde{E}\, \tilde{v}\, \tilde{j}^a(\tilde{E}) + \frac{4\pi m_a}{3} \int_0^\infty dE\, v \left(1 + \frac{V_a^2}{v^2}\right)^{3/2} j^a(E, -\mathbf{n}_\perp) \tag{4.26}$$

Using an approach similar to (4.21), we form the sum

$$\sum_k \frac{p_k}{3G} R_k(\mathbf{n}_\perp) = \sum_a \frac{m_a}{3} \int_0^\infty dE\, v \left[\sum_k \epsilon_k{}^a(E) \frac{p_k}{m_a v} \left(1 + \frac{V_a^2}{v^2}\right)^{-3/2} \right] \tag{4.27}$$

$$\left(1 + \frac{V_a^2}{v^2}\right)^{3/2} j^a(E, -\mathbf{n}_\perp)$$

Thus, if a scaling momentum p_k can be found for each channel k such that

$$\sum_k \epsilon_k{}^a(E) \frac{p_k}{m_a v} \left(1 + \frac{V_a^2}{v^2}\right)^{-3/2} < 1 \quad \text{(dominant "}a\text{")} \tag{4.28}$$

for all energies in which there is significant transverse flux for the dominant ion species, then the LHS of (4.27) exceeds the second term on the RHS of (4.26), and we have a lower bound on the average scalar pressure

$$\bar{P} > \Delta P + \sum_k \frac{4\pi p_k}{3G} R_k(\mathbf{n}_\perp) \tag{4.29}$$

where ΔP represents the sum over all species of the first integral on the RHS of (4.26), that is, the average partial pressures for energies $\tilde{E}^a$ in the plasma frame below the translation energy $m_a V_a^2/2$.

The lower bound on $\bar{P}$ used by Krimigis et al. [1981] and Lanzerotti et al. [1980] was obtained with $\Delta P = 0$, because they did not estimate the integral contribution ΔP (for $E < E_a$) which appears explicitly in (4.29) (see Sec. 4.4 and Figs. 4.18 through 4.20). As with the number density, no upper bound is offered here for the pressure because that would require a priori knowledge of the contributions of ion fluxes at energies below the lowest LEMPA channel.

By an identical line of reasoning, we can obtain an analogous lower bound on the number density because $\tilde{N}^a = N^a$.

$$N > \Delta N + 4\pi \sum_k R_k(\mathbf{n}_\perp)/G v_k \tag{4.30}$$

where ΔN represents the summed partial densities ($\tilde{E}^a < m_a V_a^2/2$). The lower bound is valid if, for all energies in which there is significant transverse flux for the dominant ion species, v_k satisfies

$$\sum_k \epsilon_k{}^a(E) \frac{v}{v_k} \left(1 + \frac{V_a^2}{v^2}\right)^{-1/2} < 1 \quad \text{(dominant "}a\text{")} \tag{4.31}$$

Thus, (4.30) with condition (4.31) provides an estimate of the lower bound on the density, independently from our other estimate (4.23), and with a different scaling condition than (4.22).

If only the sums on the RHS of (4.23) or (4.30) and (4.29) are used, they yield conservative lower bounds for N and $\bar{P}$ because $\Delta N > 0$ and $\Delta P > 0$. All bounds always exist because the conditions (4.28) or (4.22) and (4.31) can always be satisfied for large enough v_k or small enough p_k. Note that v_k and p_k are just scaling parameters that should be chosen so as to maximize the lower bounds although still satisfying the parameter conditions involving $\epsilon_k{}^a(E)$ for the significant energy ranges of all dominant ion species. They need not be related to any particular physical set (v_a, $m_a v_a$) for a given ion species, although association of the scaling velocities and momenta with those of the fastest ions actually being measured often provides valid choices.

ACKNOWLEDGMENTS

We thank the many persons at APL/JHU, the Universities of Maryland and Kansas, and Bell Laboratories for their efforts in the design, fabrication, and implementation of the LECP experiment. We are especially grateful to the LECP coinvestigators, T. P. Armstrong, W. I. Axford, C. O. Bostrom, C. Y. Fan, G. Gloeckler, E. P. Keath, and L. J. Lanzerotti, for their contributions to the hardware and analysis efforts, and to our coauthors in previous publications, J. F. Carbary, D. C. Hamilton, and R. D. Zwickl, whose efforts were essential to the overall success of the data reduction and analysis. The efforts of Voyager project personnel at JPL and at NASA Headquarters were essential to the success of the LECP program. This analysis has been supported at APL/JHU by NASA under Task I of Contract N00024-78-C-5384 between The Johns Hopkins University and the Department of the Navy and by NASA Grant NAGW-154 to The Johns Hopkins University.

5
HIGH-ENERGY PARTICLES

A. W. Schardt and C. K. Goertz

In the Jovian magnetosphere, electrons, protons, and heavier ions are accelerated to energies well above 10 MeV. These energetic particles constitute a valuable diagnostic tool for studying magnetospheric processes and produce the Jovian radio emissions. In the inner magnetosphere, both the electron and proton fluxes with energies above 1 MeV build up to $\sim 10^8$ per cm^2 s and constitute a major radiation hazard to spacecraft passing through this region. Surprisingly, high fluxes of energetic oxygen and sulfur (>7 MeV/nuc) are also found in the inner magnetosphere. Of particular interest are the interactions of these particles with the inner Jovian moons and with the Io plasma torus. Throughout much of the middle magnetosphere and magnetospheric tail, highest fluxes are found in the plasma sheet, which coincides closely with the tilted dipole equator out to 45 R_J (Jupiter radii). This plasma sheet has not been identified beyond 45 R_J in the subsolar hemisphere; however, on the night side, it extends to 200 R_J. On the day side, fluxes near the equator are relatively independent of distance (15 to 45 R_J) and fall into the range 10^4 to 10^3 per cm^2 s each for protons and electrons above ~ 1 MeV. In the predawn direction, proton and electron fluxes decrease by three orders of magnitude from 20 to 90 R_J (10^5 to 10^2 per cm^2 s) and then remain relatively constant to the boundary layer near the magnetopause. In the middle and outer magnetosphere, particle fluxes change rapidly (2 to 10 min.), and it appears that the energetic particle population is subject to a number of different dynamic processes. Jupiter is a strong source of interplanetary electrons and $\sim 10^{14}$ W are required to energize these electrons. The electron flux above 2.5 MeV in interplanetary space and in large regions of the outer magnetosphere is modulated by Jupiter's rotation period. This modulation has been ascribed to the interaction of the solar wind with a rotating longitudinal asymmetry within the Jovian magnetosphere.

5.1. Introduction

Jupiter, as the biggest planet in the solar system, also has the largest magnetosphere. In many respects this magnetosphere is quite different from that of the Earth:

1. The energy required to drive the Jovian magnetosphere is apparently extracted from Jupiter's rotational energy rather than from the solar wind as is the case for the equivalent terrestrial system. In this sense, Jupiter, as a rapid rotator (Chap. 10), may serve as a laboratory for the study of pulsar physics.
2. The Jovian magnetosphere contains several satellites and a ring that not only absorb energetic particles, but are also a source of plasma that significantly affects the structure and dynamics of the Jovian radiation belts.
3. Jupiter is a strong source of energetic charged particles that can be detected as far away as the orbit of Mercury and that carry away energy at a rate of several million megawatts (much more than the present energy consumption of terrestrial civilization). Studying Jupiter may, hence, throw some light on astrophysical acceleration processes.

On the other hand, similarities also exist with the terrestrial magnetosphere. In fact, it is surprising how successfully concepts derived from the study of the Earth's magnetosphere have been applied.